J. Jpn. Soc. Powder Powder Metallurgy, **72** (2025) S1465-S1469
https://doi.org/10.2497/jjspm.16P-T6-11

Raking and Fusing Behaviors during Fabrication of Multiple-layers in Powder Bed Fusion: An integrated discrete Element and computational thermal fluid Dynamics Study

Shuhei MINO[1]*, Masayuki OKUGAWA[1,2], Takayoshi NAKANO[1,2], and Yuichiro KOIZUMI[1,2]

[1] Division of Mater. & Manufac Sci., Graduate School of Engineering, Osaka University, 2-1 Yamadaoka, Suita, Osaka 565-0871, Japan
[2] Anisotropic Design & Additive Manufacturing Research Center, Graduate School of Engineering, Osaka University, Suita 565-0871, Japan

Abstract

In the powder bed fusion (PBF) type additive manufacturing (AM), understanding the relationship between the quality of the powder bed and the powder spreading process is crucial to avoiding defect formation. In this study, we investigated the powder-raking behavior during the multiple-layer fabrication process by discrete element method (DEM) and computational thermal-fluid dynamics (CtFD) simulations. The integrated PBF process simulation revealed that the gap height between the powder spreading blade and the build platform increases nonlinearly with the number of stacking layers, and accordingly, the powder-covered area ratio increases in the formed powder beds and affects the melt pool shapes. The powder raking behavior and melting and solidification behavior are related to each other, and both the powder raking and the irradiation conditions need to be optimized to obtain a high-quality part in the PBF process.

Keywords: additive manufacturing, powder bed fusion, discrete element method, computational thermal-fluid dynamics.

Introduction

Additive manufacturing (AM) technologies have attracted considerable attention, allowing us to easily build three-dimensional (3D) parts with complex geometries. Among the wide range of available AM techniques, powder-bed fusion (PBF) has emerged as a preferred technique for metal AM[1,2)]. In the PBF process, metal products are built layer-by-layer over thousands to tens of thousands of times by scanning laser, which fuse metal powder particles into bulk solids. The PBF enables control of the 3D shape and microstructure by controlling the process parameters. Despite these advantages, the application of PBF-type AM technology is currently limited to some aircraft parts, medical devices, and automobile parts[3)]. One reason is that the reliability of the manufactured parts is guaranteed only when a specific part is manufactured using a specific material.

The mechanical properties of PBF fabricated parts depend on their microstructure[4)] and the type and distribution of defects contained, which mainly depend on process parameters such as beam irradiation and powder spreading conditions. Inappropriate process parameters may cause defects in the manufactured parts, and the properties cannot be guaranteed[5,6)]. The process parameters must be appropriate to manufacture parts of satisfactory quality without defects using PBF[7-9)]. Therefore, understanding the influence of powder properties and spreading process conditions on the powder bed properties is important for the quality assurance of parts manufactured by PBF. Understanding these relationships allows us to optimize the conditions of the powder spreading process, improve the quality of the manufactured parts, and reduce manufacturing costs. The effects of powder properties and the spreading conditions on powder-bed qualities have been investigated. Computer simulations are effective for identifying these relationships. In particular, the discrete element method (DEM) simulation is effective, wherein the size distribution of powder particles can be set freely, and the motion of each particle and the interaction between particles can be analyzed[10-12)]. Computational analysis can reveal the powder bed formation mechanism and identify the requirements for the stable formation of a dense and highly uniform powder bed. Conversely, the beam scanning conditions are reported to affect the surface roughness in the actual PBF process [13)], and the powder raking behavior and melting and solidification behavior are suggested to be related to each other and the powder raking. The irradiation conditions must be optimized to obtain a high-quality part in the PBF process. However, the effect of the surface morphology after melting and solidification on the powder spreading behavior is not well known. It is necessary to investigate the relationship between powder properties, powder spreading conditions, and laser scanning conditions to obtain guidelines for PBF process optimization.

In this study, we investigated the powder-raking behavior during the multiple-layer fabrication process by discrete element method (DEM) and computational thermal-fluid dynamics (CtFD) simulations to identify the process optimization guidelines. We performed experiments on the angle of repose and corresponding DEM simulations to determine the interaction parameters among the particles. Thereafter, raking process simulations were performed using the determined interaction parameters, and the formed powder beds were fused with laser beam irradiations in the CtFD simulations. These simulations are repeated, and the relationships between the raking and fusing behaviors are investigated. The integrated PBF process simulation revealed that the gap height between the powder spreading blade and the build platform increases nonlinearly with the stacking layers. Accordingly, the powder-covered area ratio increases in the formed powder beds, affecting the melt pool shapes. The powder raking behavior and melting and solidification behavior are related. The powder raking and the irradiation conditions must be optimized to obtain a high-quality part in the PBF process.

Method

Experimental method

Fig. 1 shows a scanning electron microscope image and the particle size distribution of the gas atomized powder of the Ti-15Mo-5Zr-3Al alloy

*corresponding author, E-mail: shuhei.mino@mat.eng.osaka-u.ac.jp

used in this study. Ti-15Mo-5Zr-3Al alloy is a β-type titanium alloy with a body-centered cubic structure. The Ti alloy exhibits the low Young's modulus of 44.4 GPa by controlling the crystal orientation[14,15] and is expected to be used as a metal implant material. Several particles have shapes close to a true sphere, some have shapes such that a portion protrudes from a large spherical particle, and some contain satellites. The D50 of the powder is 31.9 μm. The cohesive force of these powders was estimated by dropping them through a funnel onto a petri dish and measuring the angle of repose. The funnel was filled with 50 g of powder, then dropped onto a petri dish with a 60mm diameter, placed onto an electric balance, and the angle of repose of the powder pile formed was measured. The distance between the metal funnel and the petri dish was 50 mm. The angle of repose was measured three times for each powder classification. The measured angle of repose was used to estimate the cohesive force parameter in the DEM simulation.

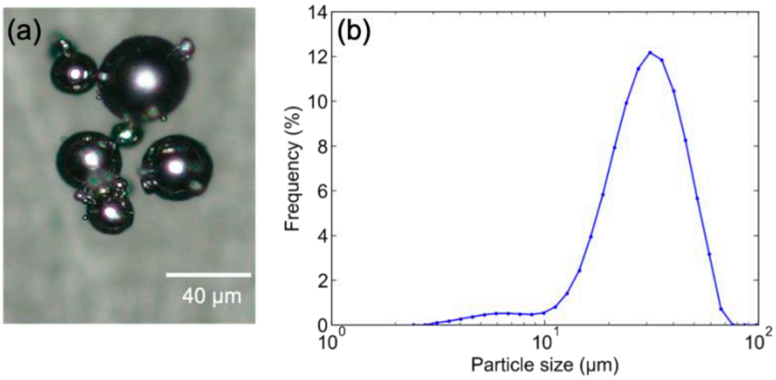

Fig.1. (a) Scanning electron microscopy image and (b) particle size distribution of gas-atomized Ti-15Mo-5Zr-3Al powder used in this study.

DEM simulations were performed using the large-scale atomic/molecular massively parallel simulator (LAMMPS) software[16]. The cohesive force causes powder agglomeration and greatly affects powder flow and packing[17] because the particle size of the powder used for AM is small at several tens of micrometers and the cohesive force becomes more dominant than gravity as particle size decreases. In this study, we adopted the Hertz-Mindlin model that includes the Johnson-Kendall-Roberts (JKR) model[18], which considers the influence of the Van der Waals forces on the contact region to add the cohesive force between powders in the contact model. The elastic force Fn in the normal direction is expressed in the JKR model as follows:

$$F_n = -4\sqrt{\pi \gamma E^*} a^{\frac{3}{2}} + \frac{4E^*}{3R^*} a^3 \qquad (1)$$

where γ is the surface energy density, and a is the radius of the contact surface. E^* is the effective Young's modulus, and R^* is the effective radius; these are expressed as follows:

$$E^* = \left(\frac{1-\nu_i^2}{E_i} + \frac{1-\nu_j^2}{E_j}\right)^{-1} \quad (2), \qquad R^* = \left(\frac{1}{R_i} + \frac{1}{R_j}\right)^{-1} \quad (3)$$

where E, ν, and R are Young's modulus, Poisson's ratio, and particle radius, respectively. In this study, the simulation was performed, assuming that the particles are true spheres. The cohesive force was estimated using γ as a fitting parameter to match the angle of repose obtained in the experiments. Particle drop simulations were performed with γ values of 7.0, 8.0, 9.0, and 10.0 mJ m^{-2}. As in the experimental setup, the powder was filled in a funnel and dropped. The simulation model was set to a 1/500 scale of the experiment owing to constraints on simulation time. The angles of repose of the formed powder piles were measured and compared with those obtained in the experiments.

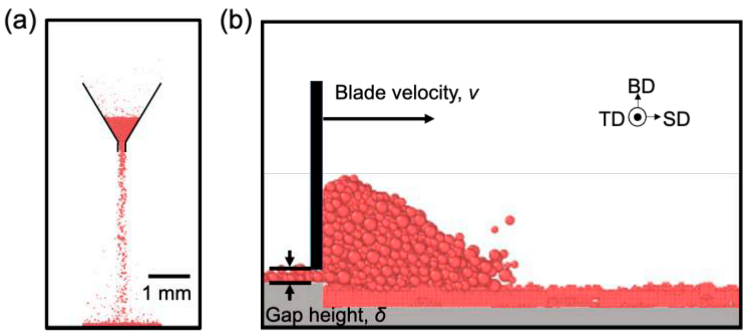

Fig.2. Snapshots of (a) powder drop and (b) powder spreading DEM simulations.

The powder raking process was simulated using the estimated γ values. Figure 2b shows a snapshot of the simulation. The y-direction was set as a periodic boundary condition. Particles were placed on the platform's edge and raked by a blade. The process conditions of blade velocity, v, and gap height, δ, were set to 150 mm s^{-1} and 60 µm, respectively.

CtFD simulations of four-track bidirectional laser-beam irradiation to the formed powder beds were performed using a 3D thermal-fluid analysis software (Flow Science FLOW-3D® with Flow-3D Weld module). Most parameters were evaluated using an alloy physical property calculation software (Sente software JMatPro v11). A uniform mesh size of 10 µm was applied throughout the computational domain. The initial temperature of the substrate was 298 K, and the atmospheric pressure was 1.013×10^5 Pa. Irradiation was performed with a beam power of P = 360 W and a scanning speed of V = 600 mm s^{-1}. The melt pool shapes and solidification conditions were evaluated based on the temperature gradient, G, solidification rate, R, and cooling rate. After the laser irradiations, the surface shapes were approximated using spherical particles, powder-spreading DEM simulations of a stacking layer were performed, and the surface roughness and particle pile-up were evaluated. Then, the multi-track laser-beam irradiation CtFD simulations were also performed to investigate the relationships between the raking and fusing behaviors.

Results and Discussion

Estimation of cohesive force by angle of repose fitting

Fig. 3a shows the powder pile formed in the powder drop experiments, for which the angle of repose was measured at 37.5° ± 0.7°. The powder pile formation was also investigated by DEM simulations, as a snapshot shown in Fig. 4b and Fig. 4c shows angles of repose of the formed powder piles obtained by the powder drop DEM simulations with various surface energy densities γ. A larger γ resulted in the formation of a larger angle of repose, and the angles of repose obtained in the particle drop experiments were reproduced when γ was 8.0 mJ m^{-2}. The determined γ value was used in the powder spreading process simulations.

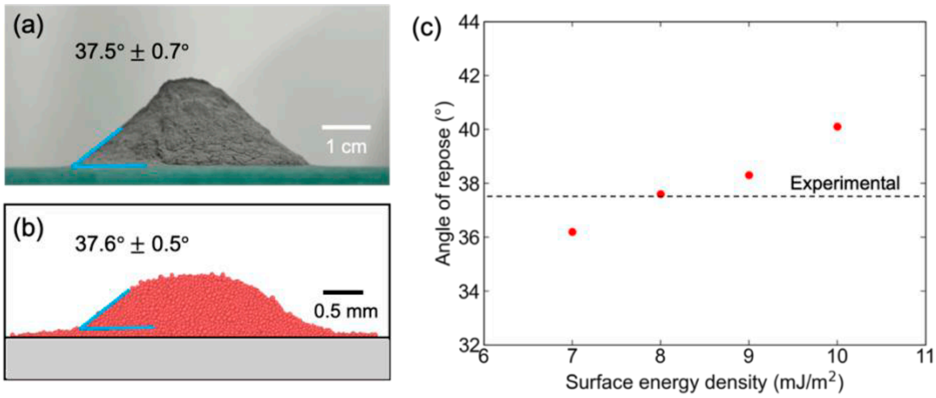

Fig. 3. (a) Optical image of cone-like pile of powder formed by pouring powder to measure the angle of repose. (b) Snapshot of the powder pile formed in powder drop DEM simulations and (c) angles of reposes obtained by the DEM simulations with various γ.

Simulations of multiple-layers fabrication

Figs. 4a1 and 4a2 show the top- and side-view images of the powder beds formed in the powder spreading simulation of the 1st layer. The particles are colored by height. The powder was distributed sparsely, and the ratio of the powder covered area was 16.9%. The ratio is smaller than that of Ti-6Al-4V[19], of which the surface energy densities γ was smaller than that of Ti-15Mo-5Zr-3Al estimated in this study. It is suggested that larger interaction between particles make its movement more difficult, resulting in the formation of the less dense powder bed.

The formed powder bed was melted and solidified by the four-track bidirectional laser-beam irradiation. Figs. 4A1–A3 show the top- and side-view of the CtFD simulated melt pool model obtained by laser irradiated to the powder bed formed by the DEM powder raked simulation. Laser beam power, P, and scanning speed, V, are 360 W and 600 mm s^{-1}, respectively. The domains are colored by the melt region. The melt pool formed by the latter laser irradiation was deeper, and this is supposed to be caused by a heat accumulation of the previous laser scanning. The surface height of the melt regions differed from place to place. The powder covered area ratio before the irradiation was only 16.9%, and the inhomogeneous in the powder bed would cause the surface roughness.

The powder spread simulation was performed again onto the laser irradiated model, and the top- and side-view images of the formed powder beds are shown in Figs. 4b1 and 4b2. Compared to the first layer, a denser powder bed formed, and the cover ratio was 36.9%. Generally, a powder bed is formed with a gap height different from the set value in the PBF process; the gap height of the first layer is the same as a set value, while the gap heights of the second and subsequent layers are greater than the set value. We previously reported that the powder spreading with a larger gap height formed a denser powder bed[19]. In the present study, the average platform height before the powder spreading of the second layer was -54 ± 5 µm, and the effective gap height was 114 ± 5 µm. The increase in the effective gap height is suggested to be caused by the increase in the cover ratio of the powder bed.

The powder bed was irradiated again, and the snapshots of the melt region are shown in Figs. 4B1–4B3. The melt pool formed by the later laser irradiation was deeper, similar to the first layer fabrication (Figs. 4A1–4A3). For comparing the fusing behaviors of the first and second layer, the melt pool formed by the laser irradiation was deeper in the second layer. On the other hand, the difference in surface height between each scanning of the second layer was smaller. The denser powder bed formed in the second layer is suggested to cause higher laser absorption and almost the same melting behavior in the entire region.

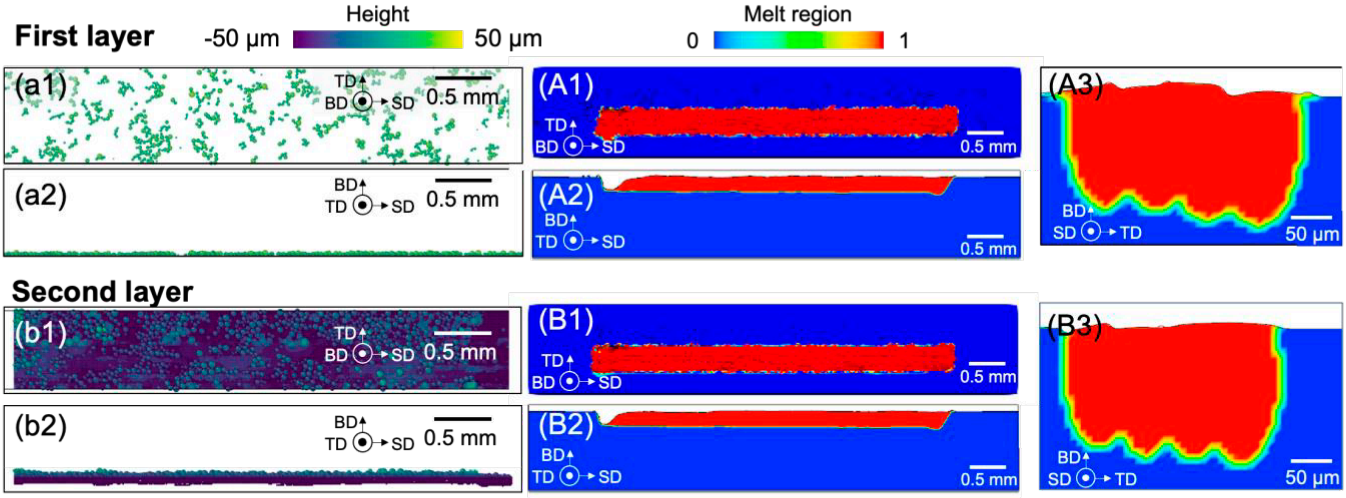

Fig. 4. Powder beds formed in the powder spreading simulations of (a1, a2) the first and (b1, b2) second layer. Snapshots of the melt region obtained by the four-track bidirectional laser-beam irradiation simulations.

Conclusions

We investigated the powder-spreading and fusing behaviors during the multiple-layer fabrication process by DEM and CtFD simulations. Compared with the first layer, the second layer had a larger effective gap height during the powder raking process. This caused the formation of a denser powder bed, which resulted in homogeneous melting in the subsequent laser irradiation process. The powder raking behavior and melting and solidification behavior are related to each other, and both the powder raking and the irradiation conditions need to be optimized to obtain a high-quality part in the PBF process.

Acknowledgements

This work was partly supported by JSPS KAKENHI Grant-in-Aid for Transformative Research Areas (A) "Creation of Materials by Super Thermal Field: Neo-3D printing by Manipulating Atomic Arrangement through Giant Potential Gradient" (Grant Numbers 21H05018 and 21H05193), The Light Metal Educational Foundation, Inc, and by CREST Nanomechanics: Elucidation of macroscale mechanical properties based on understanding nanoscale dynamics for innovative mechanical materials (Grant Number: JPMJCR2194) from the Japan Science and Technology Agency (JST).

References

1) K. Hagihara, T. Nakano: JOM. **74** (2021) 1760–1773.
2) Y. Koizumi, M. Okugawa: ISIJ Int. **62** (2022) 2183–2196.
3) Y. Koizumi, A. Chiba, N. Nomura, T. Nakano: Mater. Jpn. **56** (2017) 686–690.
4) O. Gokcekaya, T. Ishimoto, S. Hibino, J. Yasutomi, T. Narushima, T. Nakano: Acta Mater. 212 (2021) 116876.
5) S. Das: Adv. Eng. Mater. 5 (2003) 701–711.
6) J.P. Kruth, G. Levy, F. Klocke and T.H.C. Childs: CIRP Ann. **56** (2007) 730–759.
7) F.J. Gürtler, M. Karg, M. Dobler, S. Kohl, I. Tzivilsky, M. Schmidt: 25th Annu. Int. Solid Free. Fabr. Symp. An Addit. Manuf. Conf., (The University of Texas at Austin, Austin, 2014) pp. 1099–1117.
8) Y.S. Lee, W. Zhang: 26th Solid Free. Fabr. Symp., (The University of Texas at Austin, Austin, 2015) pp. 1154–1165.
9) S. Ziegelmeier, P. Christou, F. Wöllecke, C. Tuck, R. Goodridge, R. Hague, E. Krampe, E. Wintermantel: J. Mater. Process. Technol. **215** (2015) 239–250.
10) P.W. Cleary, M.L. Sawley: Appl. Math. Model. **26** (2002) 89–111.
11) Z. Xiang, M. Yin, Z. Deng, X. Mei, G. Yin: J. Manuf. Sci. Eng. Trans. **138** (2016) 1–9.
12) C. Meier, R. Weissbach, J. Weinberg, W.A. Wall, A. John Hart: Powder Technol. **343** (2019) 855–866.
13) Y. Gui, K. Aoyagi, H. Bian, A. Chiba: Addit. Manuf. **54** (2022) 102736.
14) M. Tane, K. Hagihara, M. Ueda, T. Nakano, Y. Okuda: Acta Mater. **102** (2016) 373-384.
15) S.H. Lee, M. Todai, M. Tane, K. Hagihara, H. Nakajima and T. Nakano: J. Mech. Behav. Biomed. Mater. **14** (2012) 48-54.
16) S. Plimpton: J. Comput. Phys. **117** (1995) 1–19.

17) H. Chen, Q. Wei, Y. Zhang, F. Chen, Y. Shi, W. Yan: Acta Mater. **179** (2019) 158-171.
18) K.L. Johnson, K. Kendall and A.D. Roberts: Proc. R. Soc. London. A. Math. Phys. Sci. **324** (1971) 301–313.
19) M. Okugawa, Y. Isono, Y. Koizumi, T. Nakano: Mater. Trans. 64 (2023) 37–43.

Received June 30, 2024; Revised September 17, 2024; Accepted September 26, 2024